Design and Characterization of PCB Spiral Coils for Inductive Power Transfer in Medium-Voltage Applications

Xiaotong Du, *Student Member, IEEE*, Chengmin Li, *Member, IEEE*, and Dražen Dujić, *Senior Member, IEEE*

***Abstract*—Coil design and operating frequency are key factors impacting the efficiency of the inductive power transfer system. This article presents the modeling of printed circuit board spiral coils, design optimization and analysis on coil geometry, and operating frequency for medium-voltage (MV) applications, such as auxiliary power supplies for MV converters. Analytic model considering the geometric distribution of the magnetic field is proposed to calculate with high accuracy equivalent electrical parameters of coils. For a defined design space and constraints, a large number of coils are designed to determine their performances and select optimal coil geometries. Selected coil designs are prototyped and experimentally verified under design-specific conditions. In addition, further characterization is performed considering variations of several parameters that can be encountered in practice.**

***Index Terms*—Inductive power transfer (IPT), magnetic field distribution, medium-voltage (MV) converter, modeling, printed circuit board (PCB) spiral coil.**

I. Introduction

INDUCTIVE power transfer (IPT) is a widely used technology to transfer power without physical contact in the near field. Compared to another near-field wireless power transfer technology: capacitive power transfer that transfers power by electrostatic induction, IPT relying on the power transfer by magnetic induction via the electromagnetic field can transfer power through wider physical gaps [1].

IPT technology has been applied as the power supply in various applications spanning a wide power range and a large distance range. In an IPT application, physical coil size and gap distance are the most dominant figures that limit the output power and efficiency. Applications characterized by very low power demand (< 1 W) such as biomedical implants [2] usually have a tiny size ($<1\,\mathrm{cm}^2$) and typically small gap (< 3 cm) [3], [4]. These size constraints require the IPT system to operate at megahertz (MHz) range. High power level (> 1 kW) applications, such as charging of electric vehicles (EV) [5], have relaxed restriction on coil size ($>10\,\mathrm{dm}^2$) and operating frequency is usually in the range of several tens of kilohertz. In the middle power range (1 W to 1 kW), applications include portable devices, household appliances, special industrial, and mechatronics applications. Among these applications in medium power range, the existing research articles are normally focused on the power transfer over a short gap, due to low voltages involved [6].

Considering application of auxiliary power supply in medium-voltage (MV) converters, mechanical arrangement imposes constraints on the coil size, and a large gap is typically required due to MV insulation coordination [7], [8]. Due to those restrictions of this application scenario, the large gap (>50 mm) and small coil size ($<10\,\mathrm{dm}^2$) represent the design constraint as well as challenge for the design of the IPT system.

In an IPT system, the performance of coils is one of the factors that dominate the performance of the IPT system.

The IPT coil could be in either a planar form (2-D) or 3-D structure. The 3-D structures are usually used in multitransmitter or multireceiver IPT systems [9], [10] operating at MHz range. In the single-transmitter and single-receiver system, planar coil structures are most widely used [11].

The geometry of the planar coil could be rectangular, double-D (DD), or circular. The DD shape is widely used in EV [12] because it has a better performance against lateral displacement but shows a higher power loss than the single-loop coils [13]. For applications where coils are installed in a fixed position, the lateral misalignment is not a severe problem. Therefore, the DD coil is not the optimal choice. Comparing circular spiral coils with polygonal spiral coils, the former provides a better coupling within the same surface area [14] and higher optimal quality factor [15].

The circular spiral coil could be realized with a Litz wire [16] or copper trace on the printed circuit board (PCB). The PCB tracks have much sharper edges and could challenge the dielectric design. However, PCB-based IPT as shown in Fig. 1 prevails in consistency of parameters during manufacturing and easy installation. Even though there is plenty of analysis on the PCB coil performance, PCB coil's potential in transferring a low amount of power (e.g., 150 W) over the large gap using small size coils power in MV applications is not fully explored. There are already preliminary works on the PCB coil design, including inductance, resistance, and insulation. For example, self-inductance is modeled with a current sheet method in [17],

Manuscript received May 22, 2021; revised August 23, 2021 and October 17, 2021; accepted November 20, 2021. Date of publication November 26, 2021; date of current version January 19, 2022. Recommended for publication by Associate Editor J. Acero. *(Corresponding author: Chengmin Li.)*

The authors are with Power Electronics Laboratory, École Polytechnique Fédérale de Lausanne (EPFL), 1015 Lausanne, Switzerland (e-mail: xiaotong.du@epfl.ch; chengmin.li@epfl.ch; drazen.dujic@epfl.ch).

Color versions of one or more figures in this article are available at https://doi.org/10.1109/TPEL.2021.3131013.

Digital Object Identifier 10.1109/TPEL.2021.3131013

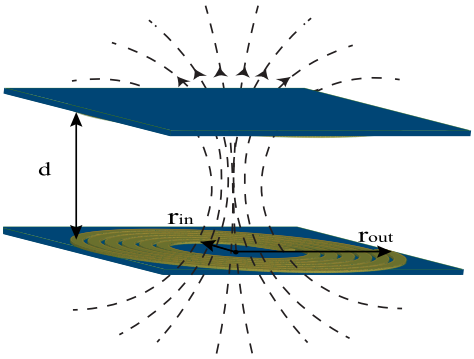

Fig. 1. Example of using PCB spiral coils to realize IPT through air. Primary and secondary coils are placed face to face. d is the air gap between the primary and secondary coils. r_{in} and r_{out} are the inner and outer radius of the primary coil. The secondary coil could have a different geometry from the primary coil.

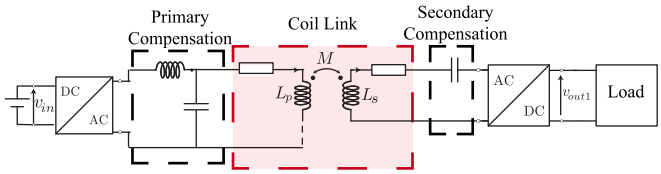

Fig. 2. Structure of auxiliary power supply for MV converters. Multiple series connected coils are usually used but only one pair of the coil is shown for the illustration.

TABLE I
DESIGN SPECIFICATIONS

V_{in}	V_{out}	$U_{ins-rms}$	P_{out}	$thickness$
80 V	$36 \pm 2V$	6 kV	150 W	70μm

which has a large error when space between traces is much larger than trace width. The ac resistance model is given in [18], which needs finite-element modeling (FEM) simulation to obtain a magnetic field. Authors of [16] have studied on the insulation with air, while in [19], insulation has been analyzed with solid dielectric materials including FR4, Polyesterimide, and Teflon. However, no systematic design approach for PCB coils could be identified. This article's main purpose is to present a systematic and generalized model-based design approach that outputs a database and from which users could select coils based on their own needs and preference. The optimization approach offers several insights in designing IPT coils and considering air (at least in present work) as the only dielectric material between the transmitter and receiver. First, the optimization approach explores the system performance in a wide range of coil geometries and the tradeoff between the power density and efficiency is clearly demonstrated. Second, the influence of the operating frequency on the performance of the coil pairs is shown, which permits selecting an optimal frequency, for the further system design. Finally, for the selected and prototyped coils, the limits of the coil geometry to transfer a certain amount of power are determined through experimental characterization considering variation of distance between the coils as well as minor misalignment that would occur in practice. The complete IPT system would naturally include primary and secondary side power electronics stages, however, optimization of these is outside the scope of this article.

The rest of this article is organized as follows. In Section II, a design space considering specifications of typical MV application is defined. In Section III, an analytic model considering the magnetic field's geometric distribution is proposed to calculate the coil's equivalent electric parameters with a high speed and high accuracy. FEM simulations using ANSYS Maxwell are used for the validation of modeling. In Section IV, a large number of coils are designed over the design space and their performances are explored considering defined constraints. In Section V, experimental results are presented, obtained from the selected and prototyped coils. Section VI presents further performance characterization results of the same coils under an extended operating condition range. Finally, Section VII concludes this article.

II. IPT DESIGN SPACE

An IPT system is usually composed of compensation networks, transmitter coil, and receiver coil. The optimization of the coil geometry in an IPT system is depending on the operation mode of the compensation network. Various compensation networks are proposed for different application needs, including simple compensation (series–parallel, series–series, parallel–parallel, parallel–series) and hybrid compensation networks (*LCL, LLC*, etc.) [20]. Choice of compensation network leads to different transfer ratios, and therefore, different optimization results.

The optimization approach proposed in this article is generalized that holds the same workflow for different compensation strategies. The different typologies and inputs influence only the filtering criteria. In this article, the LCL-S compensation network as shown in Fig. 2 is considered [21].

The optimization approach is also based on the specific electric inputs and outputs of one application scenario. In this article, the electric outputs are set for the auxiliary power supply considering the MV converters application case. While the general MV range up to 36 kV is considered as relevant, a 6-kV system working voltage is taken as the case in this article to illustrate the optimization approach. The insulation distance is defined based on this voltage from the standard IEC 61800-5-1 [22]. Other electric specifications used for the application considered in this article are listed, respectively, in Table I. Output dc voltage of 36 ± 2 V is defined as reference, which could be further regulated with additional converters for supplying various auxiliary voltages in MV converters. Similarly, 150-W output is considered as reasonable maximum power level demand for one power electronics building block in MV converters, including gate drivers, controllers, cooling fan, etc.

Considering the tradeoff between the low switching loss on power electronics switches and high efficiency on coil links, operating range is taken from 50 kHz to 1 MHz. Considering

TABLE II
DESIGN SPACE OF PCB COIL GEOMETRIES AND OPERATING FREQUENCY

Sweeping inputs	Characteristics	Value/Range	Units
Outer radius	r_{outp}, r_{outs}	10-75	mm
Copper trace width	w_p, w_s	1-20	mm
Space between adjacent copper turns	s_p, s_s	1-20	mm
Number of turns of one coil	n_p, n_s	$max = \frac{Rout}{w+s}$	-
Operating frequency	f	50-1000	kHz

the mechanical constraints in typical MV converter assembly, a maximum coil diameter is restricted to 150 mm. The geometries range studied in this article are shown in Table II.

It should be noted that both the electric specifications and coil geometries restriction should be changed according to application requirements. Nevertheless, the proposed analytic model and optimization approach is generalized and can be adapted in other application scenarios.

III. PCB SPIRAL COIL MODELING

The accurate mathematical model of inductance and resistance is the basis for designing coils. In this section, the magnetic field is first mathematically modeled, followed by the modeling of self-inductance, ac resistance, and mutual inductance.

A. Modeling of External Magnetic Field

One of the common methods used in solving magnetic fields is to solve Maxwell's equations for rectangular cross sections by dealing with numerical integration [23]. Despite being slow and complicated, this method gives precise results. Another popular approach is the filament method, which considers coil as a dimensionless filament of negligible cross section [24]. It gives a closed-form equation but has larger errors when the cross-sectional dimension is large. Here, a modified filament method is proposed, using two current loops on conductor edges to represent the current in one turn circular conductor. The proposed method intends to have smaller errors while keeping the calculation's simplicity.

The cross section of the PCB-based spiral coil is illustrated in Fig. 3. For simplicity, coaxial circles are typically used instead of a spiral structure [19], [25]. The external magnetic field H_{ex} in the ith turn defined as $H_{\text{ex},i,\text{tot}}$ refers to the magnetic field caused by current in other turns excluding the magnetic field caused by its own current [26].

$$H_{\text{ex},i,\text{tot}} = \sum_{k=1}^{N} H_{i,k},\ k \neq i. \tag{1}$$

Three simplifications are made in obtaining an analytic model. First, since the thickness of the coil t is rather small (commonly used PCB thickness is 35 µ or 70 µm), the external H field parallel along the e_x axis is ignored, and only the magnetic field in the e_z direction is considered. Second, since in the defined frequency range (50 kHz–1 MHz), the skin depth is at least three times smaller than trace width in the design space ($\geq$ 1 mm),

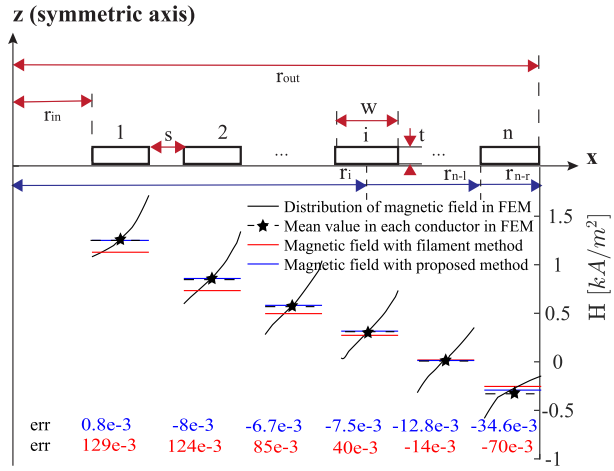

Fig. 3. Concentric circular conductors with rectangular cross sections and magnetic field distribution with a current excitation of 1 A at 500 kHz for a six-turn coil with $w = 5\,\text{mm}, t = 0.07\,\text{mm}$, and $R_{\text{out}} = 70\,\text{mm}$. The errors are absolute errors: err = modeling result—mean value of simulation result.

current in one trace is simplified to two dimensionless current loops at left and right edges. Third, the nonuniform distribution of the magnetic field inside the track is simplified to be constant and is represented by the magnetic field at the center point of the track. Taking the nth turn as an example, the average magnetic field in the ith turn caused by the nth turn, as shown in Fig. 3 is [26]

$$H_{\text{ex},i,n} = \frac{1}{\mu_0}\frac{\mu I_l}{4\pi}\frac{1}{r_{n-l}+r_i}\left[K(k_l) + \frac{r_{n-l}^2 - r_i^2}{(r_{n-l}-r_i)^2}E(k_l)\right] + \frac{1}{\mu_0}\frac{\mu I_r}{4\pi}\frac{1}{r_{n-r}+r_i}\left[K(k_r) + \frac{r_{n-r}^2 - r_i^2}{(r_{n-r}-r_i)^2}E(k_r)\right]. \tag{2}$$

In the aforementioned equation, I_l and I_r are the current on the left and the right edge, respectively. $K(k)$ and $E(k)$ are the complete elliptical integrals of first and second kind to modulus k.

$${k_{l/r}}^2 = \frac{4r_{n-l/r}r - i}{(R+p)^2}. \tag{3}$$

In order to get I_l and I_r, two steps are followed. First, currents are supposed to be equally concentrated on the left and the right edge $I_l = I_r = \frac{I}{2}$, where I is the total current inside the conductor. Initial magnetic field is obtained with (2). The electric field distribution along the x-axis is

$$\frac{\partial E_y}{\partial x} = -j\omega\mu\text{H}. \tag{4}$$

Furthermore, $J_{\text{prox-edge}}$, the current density at both edges under the external magnetic field is obtained

$$|J_{\text{prox-edge}}| = -j\omega\mu\frac{w}{2}\sigma H. \tag{5}$$

In this equation, ω is the angular frequency of current excitation, μ is the magnetic permeability of copper, which is $4\pi e^{-7}$, w is the width of the copper trace, σ is the conductivity of copper, and H is the external magnetic field.

The current at both edges under the skin effect is approximated as

$$J_{\text{skin-edge}} = \frac{I}{2t\delta} \tag{6}$$

where t is the thickness of copper trace and δ is the skin depth. Finally, the current density on both edges is the result of two effects

$$\begin{aligned} J_{\text{edge-left}} &= J_{\text{skin-edge}} + J_{\text{prox-edge}} \\ J_{\text{edge-right}} &= J_{\text{skin-edge}} - J_{\text{prox-edge}}. \end{aligned} \tag{7}$$

Under the filament approximation, the summation of the left edge current I_l and right edge current I_r is the entire current I. Current distribution is supposed to be

$$\begin{aligned} I_l &= I\frac{J_{\text{edge-left}}}{J_{\text{edge-left}} + J_{\text{edge-right}}} \\ I_r &= I\frac{J_{\text{edge-right}}}{J_{\text{edge-left}} + J_{\text{edge-right}}}. \end{aligned} \tag{8}$$

Finally, the magnetic field is solved with (2) and (8).

Comparing to the original filament method, the proposed method considers two current loops at edges instead of one current loop in middle of the conductor trace. Besides, the proposed method considers the redistribution of the magnetic field with the knowledge of current density distribution. The accuracy of the proposed approach is validated with the randomly selected coil geometry against FEM simulations. In Fig. 3, the result of a spiral coil of six turns with $w = 5\,\text{mm}, t = 0.07\,\text{mm},$ and $R_{\text{out}} = 70\,\text{mm}$ is shown. The real magnetic field distribution is not linear. Comparing to the result with the filament method from [24], the result of the proposed method better presents the mean value of the real distribution.

B. Modeling of Self-Inductance

The current sheet method is commonly used for modeling the inductance, which considers multiple spiral turns as one single current sheet [17]. However, the error increases when the ratio between s and w is bigger than 3. The data-fitting technique for a predefined monomial model is also an option [17], but the existing model is only for polygonal spiral coils, not for circular coils.

In this section, the spiral coil is modeled as coaxial circular conductors. The inductance of the circular spiral coil can be expressed as the sum of self-inductance of each circular sheet and mutual inductance between each pair of sheets. This method intends to avoid error caused by large space between turns.

$$L_{\text{spiral}} = \sum_i L_i + \sum_{i,j} M_{i,j}\ \forall i, j \in n. \tag{9}$$

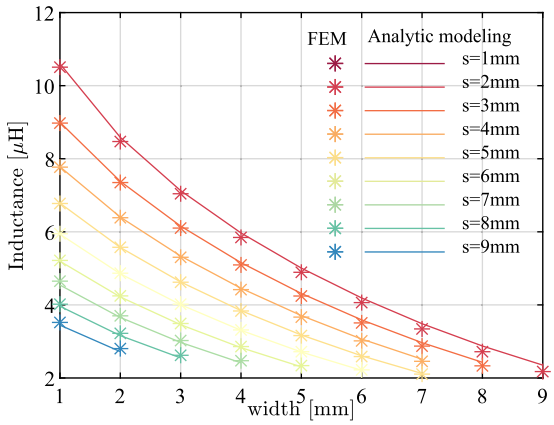

Fig. 4. Inductance extracted from FEM simulation and from analytic modeling. The studied coil has six turns and an outer radius of 75 mm. The trace width and space between turns vary with a step of 1 mm.

This summation method works for all the s and w ranges. The self-inductance and mutual inductance in (9) are [15], [27]

$$\begin{aligned} L_i &= \mu r_i \left[\ln\left(\frac{2r_i}{w}\right) + 0.9 + 0.05\frac{w^2}{r_i^2}\right] \\ M_{i,j} &= \frac{\mu(r_i + r_j))}{2}\left[\ln\left(\frac{r_i + r_j}{w + s}\right) - 0.6 + 0.7\left(\frac{w+s}{r_i + r_j}\right)^2\right] \\ &\quad + \left(0.2 + \frac{(r_i + r_j)^2}{12(w+s)^2}\right)\frac{\mu\omega^2}{2(r_i + r_j)}. \end{aligned} \tag{10}$$

Again, the analytic model of the PCB coil inductance are checked against the FEM simulations for randomly selected coil geometries. Fig. 4 shows the inductances extracted from ANSYS Maxwell 3-D and analytic modeling for the coils with six turns and outer radius of 75 mm ($R_{\text{out}} = 75$ mm). With the constraints of outer radius and number of turns, the maximum trace width is $9\,\text{mm}$. Trace width and space between turns are swept to generate more designs. According to Fig. 4, the analytic result correlates well with the FEM result for all considered coil geometries.

C. Modeling of AC Resistance

Unlike the traditional inductor design, there is no empirical model calculating the resistance of PCB spiral coils. Besides, unlike a circular cross-sectional conductor [28], there is no closed-form analytic expression to calculate the resistance of a rectangular cross-sectional coil. Therefore, a hybrid FEM database and magnetic field calculation method is proposed in order to increase the accuracy in resistance calculation.

1) Orthogonality of Conduction and Proximity Losses: As shown in Fig. 5, in the rectangular cross-sectional conductors, the independence of conduction and proximity losses remains as in the round wires. First, the superposition of current densities due to skin effect and proximity effect is involved. The total loss

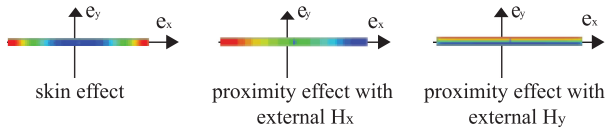

Fig. 5. Current density distribution caused by skin effect, proximity effect in a conductor track with rectangular cross section, and infinite long in the e_z direction.

P_{ac} for unit length can be calculated as follows:

$$P_{\text{ac}} = \frac{1}{2\sigma}\int_S (J_{\text{cond}} + J_{\text{prox},x} + J_{\text{prox},y}) \times (J_{\text{cond}} + J_{\text{prox},x} + J_{\text{prox},y})^* dS. \tag{11}$$

In the aforementioned equation, all the cross-term products are zero. Therefore, (11) can be simplified as the superposition of conduction losses (caused by the influence inside the conductor including skin effect loss under high frequency excitation) and proximity loss (caused by the influence of other conductors).

$$P_{\text{ac}} = \frac{1}{2\sigma}\int_S \left(J_{\text{cond}}J^*_{\text{cond}} + J_{\text{prox},x}J^*_{\text{prox},x} + J_{\text{prox},y}J^*_{\text{prox},y}\right) dS. \tag{12}$$

2) FEM Database to Evaluate Resistance: In rectangular cross-sectional conductors, expressions to evaluate both types of losses are given in [18]

$$\begin{aligned} R_{\text{cond}u.l.} &= \frac{1}{whs}\Phi_{\text{cond rec}}(w/\delta, h/\delta) \\ R_{\text{prox}u.l.x} &= \frac{4\pi}{\sigma}\Phi_{\text{prox rec}}(w/\delta, h/\delta)\hat{H}^2_{1,x} \\ R_{\text{prox}u.l.y} &= \frac{4\pi}{\sigma}\Phi_{\text{prox rec}}(w/\delta, h/\delta)\hat{H}^2_{1,y} \end{aligned} \tag{13}$$

where $H_{1,x}$ and $H_{1,y}$ are the magnetic field generated by the 1 A current and are calculated with a magnetic field model in Section III-A. Φ are dimensionless functions that describe frequency and geometry dependence of resistance. With current I through the spiral coil, the power loss is

$$P_{\text{ac},u.l.} = \frac{1}{2}(R_{\text{cond}u.l.} + R_{\text{prox}u.l.x} + R_{\text{prox}u.l.y})I^2. \tag{14}$$

Since Φ_{cond} and Φ_{prox} in (13) do not have closed-form analytic expressions, FEM is used to calculate the value of these functions. In ANSYS Maxwell 2-D, the conductor is modeled as a straight conductor with infinite length. The geometry and frequency are swept according to Table II. In addition, copper thickness t is swept from 0.035 to 0.21 mm.

It has to be noted that FEM is only used to generate database for Φ in (13) rather than directly for ac resistance because Φ has fewer free dimensions and requires a much smaller database.

In Fig. 6(a) and 6(b), the x-axis $w/\delta \cdot h/\delta$ is the cross-sectional area of the conductor with respect to the effective conducting area. The value smaller than 1 means the frequency effect can be ignored. The bigger value means the stronger influence of the high frequency on the effective conducting area. The y-axis w/h represents the form factor of the cross section, with the value close to 1, the cross section is close to a square

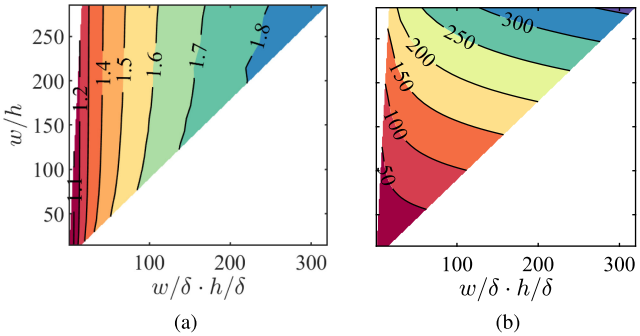

Fig. 6. Dimensionless functions extracted from FEM simulation. (a) Φ_{cond}. (b) Φ_{prox}. Φ_{cond} is obtained by setting a current excitation through a straight conductor. Balloon boundary is set at the region edges. Φ_{prox} is obtained by setting a constant magnetic field in the e_y direction. Variant magnetic vector potential is set at the simulation region edges.

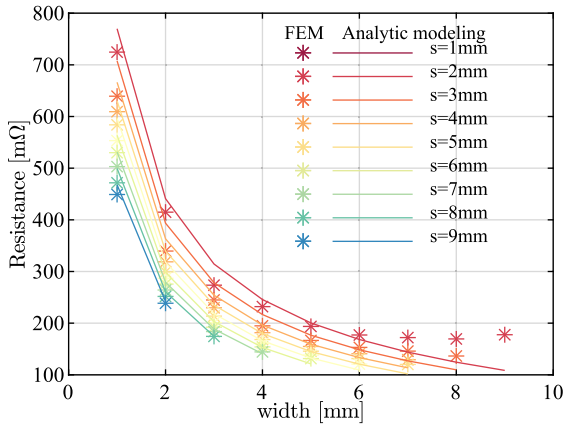

Fig. 7. Resistance at 500 kHz extracted directly from FEM simulation and from analytic calculation in (13). The studied coil has six turns and an outer radius of 75 mm. The trace width and space between turns vary with a step of 1 mm.

area. The function model can be obtained by importing these data into MATLAB and using the curve fitting tool. In the curve fitting tool, the x, y, and z data in wFig. 6 are taken as inputs to train the model. The output of the curve fitting tool is a dimensionless function Φ. In this manuscript, our function is obtained with the biharmonic interpolation method.

3) FEM Verification: The modeling of resistance of the spiral coil is verified with the same case for self-inductance verification. As shown in Fig. 7, the modeling matches well with the FEM results in most cases. With the increase of the trace width ($w > 8$ mm), the error becomes larger, which results from the simplification while modeling the magnetic field as well as the simplification by using concentric circles instead of spiral coils. However, considering that in reality, very wide PCB traces are rarely used in spiral coils, the proposed fast modeling of resistances is still applicable in most cases.

D. Modeling of Mutual Inductance

Power transfer requires at least two coils. As shown in Fig. 8, in this article, two coils are placed face to face on the primary side

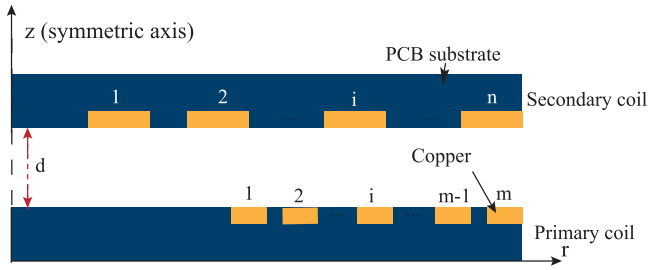

Fig. 8. Set of IPT PCB coils in the z-plane. Copper trace on the outer layer of the PCB is the focus of this article and the PCB substrate design is not discussed here. The air gap between the primary coil and secondary coil is d. For illustration purpose, the primary coil has m turns and secondary coil has n turns.

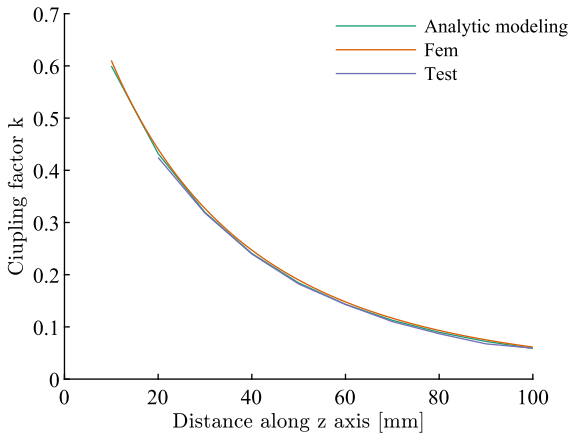

Fig. 9. Coupling between two coils: the primary coil has six turns, turns width of 5.2 mm, turns gap of 2 mm, and outer radius of 70 mm; the secondary coil has seven turns, turns width of 2 mm, turns gap of 1 mm, and outer radius of 70 mm.

and secondary side, respectively with air between them. In MV application, the smallest distance d between them is determined by the insulation voltage taking into account type of insulation, overvoltage category, and pollution degree. Mutual inductance is calculated based on the method in [29], where the planar spiral coils are simplified to cocentral loops and mutual inductance M is calculated as the summation of mutual inductance between each circular loops.

$$M = \sum_{i=1}^{M} \sum_{j=1}^{N} M_{i,j}(r_i, r_j, d). \tag{15}$$

As shown in Fig. 8, i and j are, respectively, ith and jth turn in primary and secondary coils.

Two coils are fabricated and taken under test with a different air gap between the two coils. The test result, the calculation result, and FEM results are shown in Fig. 9. The three curves superposed each other well. The coupling factor shows a clear decline with a longer distance.

IV. Design Process

In this section, the performance of various coil geometries within the design space in Table II are evaluated based on

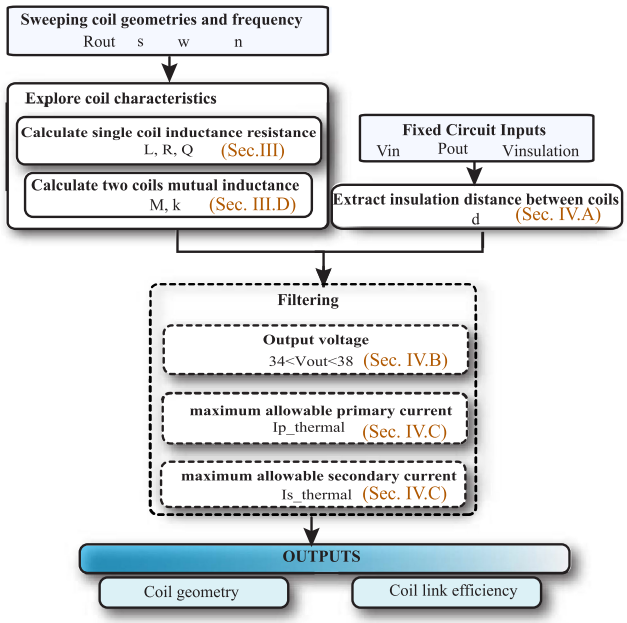

Fig. 10. Design procedure followed in this article to optimize coil pairs in the IPT system. The output of this procedure is all the possible primary and secondary coil geometries that meet application requirements. The variable notations in this flow chart correspond to those in Section II. For each design step, the corresponding article section is listed.

the aforementioned mathematical model. The design procedure shown in Fig. 10 is based on brute-force search in the entire design space. Before the start of the design approach, the distance between primary and secondary coils in the IPT system should be defined and this is addressed in detail thereafter in Section IV-A. In the design procedure, first, individual coils are characterized with the inductance model and resistance model proposed in Section III. Second, coils are grouped into pairs, considering all the combinations. Mutual inductance of each pair is calculated with the analytic model in Section III and based on the coil distance. Third, the power transfer capability of each coil pair is evaluated as illustrated, thereafter, in Section IV-B. Finally, designs are filtered by the constraints illustrated in Section IV-C.

Various coils within the design space in Table II are evaluated based on the analytic modeling. The width of copper trace is swept from 1 to 20 mm, the space between spiral turns is swept from 1 to 20 mm and the outer radius of the circular coil is swept from 10 to 75 mm. The minimum space of 1 mm is taken to avoid an electric breakdown between coil turns according to the IPC9592 standard. For these ranges, ten equal steps are used in between. The number of turns is from 1 to the maximum allowable turns with defined w, r_{out}, and s. Each set of these variables characterize uniquely each single coil. In one coil pair, the primary and secondary do not need to be identical. In total, 1426 single coils with different geometries are designed and 1426^2 combination of coil pairs are explored considering 11 different operating frequencies. With 4 Intel i7 cores, 16-GB RAM, it took 24 h to finish the calculation of all the coils. The inductance and resistance of coils are obtained by modeling, namely, L_p, L_s, R_p, R_s, and M. The figure of merits coupling

TABLE III
MINIMUM CLEARANCE DISTANCE REQUIRED TO PROVIDE BASIC INSULATION

System working voltage	6 kV	Minimum clearance distance	28.4 mm
Impulse voltage of overvoltage category II	24.8 kV	Minimum clearance distance	32.8 mm
Temporary overvoltage	24 kV	Minimum clearance distance	54.84 mm

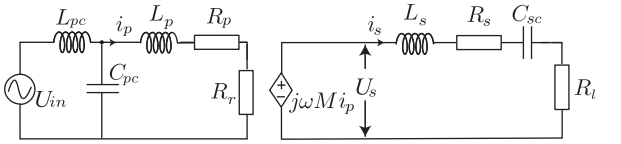

Fig. 11. Equivalent model of the IPT system with LCL-S compensation network.

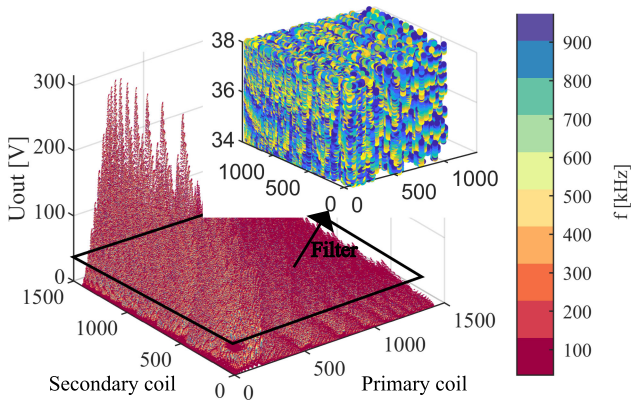

Fig. 12. Output voltages of all the coil combinations. In total, $1426^2 \times 11$ designs are shown. After filtering by design constraints, 18 868 designs are left and are shown in the zoom-in view.

factor and quality factor are defined as $k = \frac{M}{\sqrt{(L_p L_s)}}$, $Q_p = \frac{\omega L_p}{R_p}$, and $Q_s = \frac{\omega L_s}{R_s}$. Furthermore, the current through coils, output voltage over the secondary coil, and coil link efficiency are calculated.

A. Insulation Distance

Insulation distance is determined by interpolation from standard IEC 61800-5-1 [22, Tables 8 and 9]. The clearance distance for basic insulation between two coils is defined according to the working voltage, the impulse voltage, the temporary overvoltage, and the recurring peak value of the working voltage. As shown in Table III, the rms value of working voltage is 6 kV. The impulse voltage and temporary overvoltage are determined by this working voltage. The impulse voltage also depends on the overvoltage category. With the overvoltage category II, the impulse voltage is 24.8 kV, and temporary overvoltage is 24 kV. The final clearance distance takes the maximum value among the three distances. However, in practical design considering the complex environment, an extra safety margin is always recommended. Finally, 60 mm is taken as the distance between two coils to realize basic insulation for the 6 kV system. It should be noted that the standard used to define insulation distance should be selected based on different applications.

B. Outputs of Coil Links

In this section, ac voltages and currents are all in rms values, and the subscript p refers to the primary side, while s indicates the secondary side. Equivalent model of the coil link is shown in Fig. 11. The coil link efficiency is the product of the efficiency of the primary side and secondary side

$$\eta_{\text{coil link}} = \eta_p \eta_s = \frac{R_r}{R_r + R_p} \frac{R_l}{R_l + R_s} \tag{16}$$

where $R_r = \frac{\omega^2 M^2}{R_l + R_s}$ is the reflected resistance of secondary on the primary side. R_l is the equivalent load. Provided ideal compensation [21], R_l is obtained by solving the equation of the output power

$$\frac{U_s^2}{(R_s + R_l)^2} R_l = P_{\text{out}} \tag{17}$$

where R_s is the resistance of the secondary coil. By solving (17), the load resistance is

$$R_l = \left(\frac{U_s^2}{P_{\text{out}}} - 2R_s \right) + \frac{\sqrt{(\frac{U_s^2}{P_{\text{out}}} - 2R_s)^2 - 4R_s^2}}{2}. \tag{18}$$

Finally, the dc output voltage after the half-bridge rectifier is obtained

$$U_{\text{dc}} = \frac{\pi}{\sqrt{2}} \frac{U_s R_{\text{load}}}{R_{\text{load}} + R_s}. \tag{19}$$

C. Design Constraints

By pairing all possible coil pairs, different relations are generated between input and output voltage. The output voltage for each coil pair is shown in Fig. 12, with many combinations producing output voltage outside the desired range. Useful coil pairs need to be extracted for the analysis. With the current and voltage outputs obtained in the previous section, the coil designs are filtered by two criteria, namely the output voltage range and heat dissipation limit.

The output voltage at the rated power is limited in the range 34–38V. The coil pairs that violate this voltage range are filtered out and not analyzed further.

Regarding heat dissipation, natural convection is considered in this work. With natural cooling, thermal resistances are shown in Table IV.

Since $\theta_{\text{Cu}} \ll \theta_{\text{SA}}$, the thermal resistance of the primary and secondary coil are dominated by the copper coverage surface $\pi(R_{\text{out}}^2 - R_{\text{in}}^2)$ and copper thermal resistance θ_{SA}. Since the thickness of FR4 is minimal (≈ 1.55 mm), the heat is approximately dissipated equally through both sides of the PCB board,

TABLE IV
THERMAL RESISTANCE OF THE PCB COIL

Name	Value	Description
θ_{Cu}	$0.25\frac{^\circ Ccm^2}{W}$	Thermal resistance of $1cm^2$ copper
θ_{FR4}	$67.43\frac{^\circ Ccm^2}{W}$	Thermal resistance of FR4 substrate in $1cm^2$ and thickness of $0.155cm$
θ_{SA}	$1000\frac{^\circ Ccm^2}{W}$	Thermal resistance from $1cm^2$ PCB surface to air

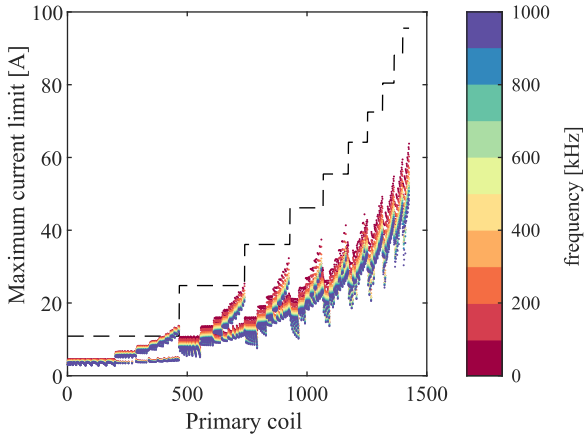

Fig. 13. Two different current limitations: black dashed represents the current limitation extracted from the standard IPC-2221 [30]; colorful dots represent the current limit calculated by conductor loss. Four parameters are swept from the inner loop to outer loop following the order: $n, r_{\text{out}}, s,$ and w. Four parameters increase as the coil numbering rises.

thus

$$R_{\text{th}} = R_{\text{th}-\text{uppersurface}} + R_{th-\text{lowersurface}} = \frac{\theta_{\text{SA}}}{\pi(R_{\text{out}}^2 - R_{\text{in}}^2)} \frac{1}{1+\frac{1000}{1067}} \frac{w}{w+s}. \quad (20)$$

The current limited by the heat dissipation capability is

$$I_{\text{cal}} = \sqrt{\frac{\triangle T}{R_{\text{th}} R_{\text{coil}}}} \quad (21)$$

where R_{coil} is the resistance of coil obtained from analytic modeling; and $\triangle T$ is the allowed temperature rise. Another current restriction comes from standard IPC-2221 [30], where the same current limit are used under variant current excitation frequency. By curve fitting, the maximum current in the external copper layer is

$$I_{\text{std}} = (\text{width} \cdot \text{thickness})^{0.725} 0.048 \triangle T^{0.44}. \quad (22)$$

The current limited by thermal dissipation capability takes the minimum value between the I_{std} and I_{cal}. The comparison of I_{std} and I_{cal} is shown in Fig. 13 . I_{std} extracted from the standard is usually higher than the calculated value I_{cal}.

V. RESULTS OF OPTIMIZATION TOOL

In the entire design space in Table II, $1426^2 \times 11$ coil pair designs were explored.

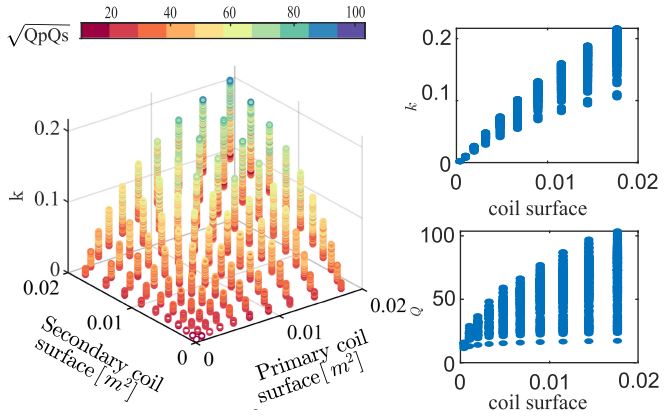

Fig. 14. Relation between the coil surface area, coupling factor, and quality factor. The 3-D view is on left. On the right, 2-D plots are shown with identical primary and secondary coils.

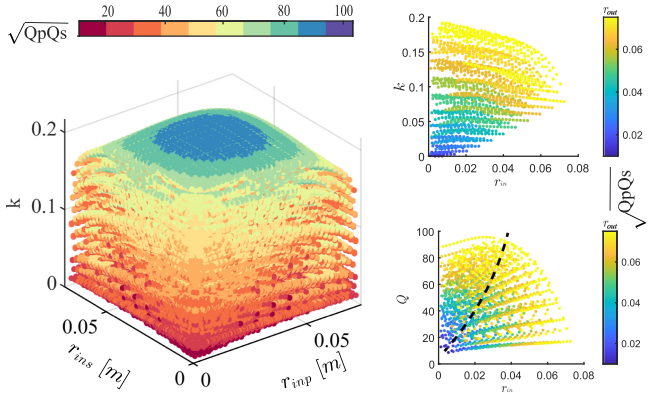

Fig. 15. Relation between the coil inner radius, coupling factor, and quality factor. The 3-D view is on left. On the right, 2-D plots are shown with identical primary and secondary coils.

A. *Influence of Coil Geometry*

High coupling factor k and high quality factor Q_p, Q_s are the figure of merits to achieve a high coil link efficiency. Therefore, they are considered as the main performance indicators for coils. In this section, several important coil geometry properties are explored. Their influence on k, Q, and coil link efficiency are analyzed. The results shown in this section are all at an operating frequency of 500 kHz.

1) Surface Area of Coil: The surface area here is defined only by coils' outer radius and omits the differences of the inner radius since the outer radius defines the final size of the coil. The surface area dominates the coupling factors between two coils and the quality factor of a single coil. As shown in Fig. 14, when the surface area increases, the maximum reachable k and Q also increase. A large outer radius also brings a high achievable efficiency.

2) Inner Radius of Coil: To minimize eddy current effects and get higher coupling, majority of previous studies recommend to eliminate the most inner turns by leaving a hole in the middle of the spiral coil [25], [31]. The dependence on the coil inner radius of k and Q are presented in Fig. 15. The 3-D plot

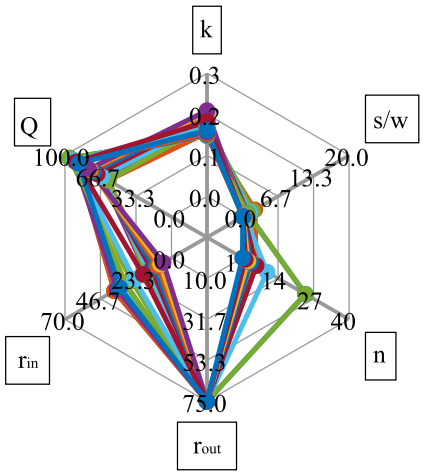

Fig. 16. Radar plot for designs in 500 kHz with two optimal goal k, Q as well as interesting parameters in each leg. Each color represents one design.

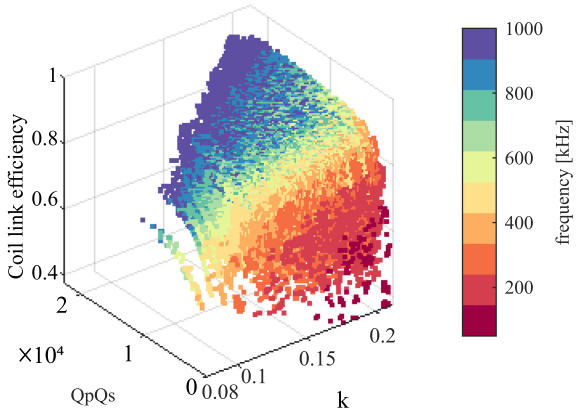

Fig. 17. Relation between frequency, coupling factor k, quality factor Q_pQ_s, and coil link efficiency. Higher frequency leads to higher Q in the defined frequency range. The designs that have a small k show stronger limit on achievable maximum Q. Higher k and Q lead to higher efficiency.

includes the consideration of combinations of different primary and secondary coils. On the other hand, the 2-D plot considers only the combination of identical primary and secondary coils. From the 2-D plots, it is apparent that Q is expected to drop sharply after the peak. With the decrease in different outer radius, the optimal inner radius for the peak Q is decreasing. For the ten outer radius [10, 17.2, 24.4, 31.7, 38.9, 46.1, 53.3, 60.6, 67.8 75], the corresponding inner radius to achieve highest Q are [5, 8.2, 11.4, 14.6, 17.9, 21.1, 24.3, 27.6, 30.8, 36]. The units are in millimeters.

3) Space-Width Ratio: The space between each turn affects Q. A narrow space brings a higher inductance, but it also means a stronger proximity effect leading to a higher coil resistance. Therefore, an optimal range exists to achieve a maximum Q. Based on our database, $\frac{s}{w} \leq 1.5$ is a reasonable optimal range.

4) Number of Turns and Trace Width of Coil: Based on our dataset, the optimal w to achieve Q and k are scattered over the entire design space. For the turns number n, there is no general optimal range to achieve maximum k. On the other hand, coil composed of a single turn ($n = 1$) has prominent high Q.

5) Conclusion: In order to see the optimal design range of each geometry parameter, a radar plot is shown in Fig. 16, where each leg of the radar is a different design parameter. The design points on each leg defines the optimal range for this parameter. For example, the outer radii are all at 75 mm, the $\frac{s}{w}$ ratio is less than 2, the inner radius and turns number are scattered in a larger range in the design space, and no optimal design range is observed. This shows that the larger the outer radius, the higher the performance. And $\frac{s}{w}$ is a delicate parameter, which has a upper limit of the optimal design range.

B. Influence of Operating Frequency

The results discussed in this section consider only the filtered designs. In Fig. 17, there is a clear trend that in the defined frequency range, the quality factor increases as the frequency increases, which is explained as the increase of coil resistance caused by high frequency is not comparable to the increase of inductive reactance.

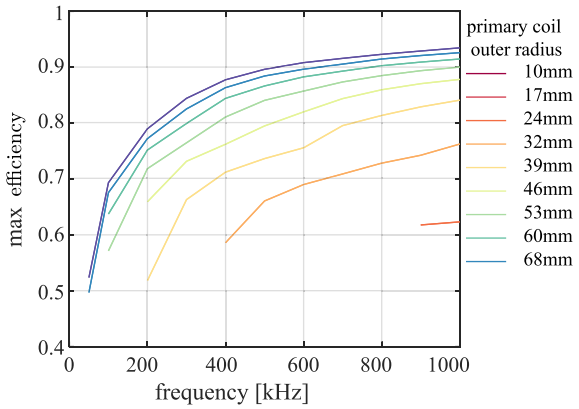

Fig. 18. Maximum achievable coil link efficiency under different operating frequencies and different outer radius within the design space.

In Fig. 18, although the maximum attainable coil link efficiency increases as the frequency keeps increasing, 500 kHz is chosen over 1 MHz for the experimental demonstration thereafter. Because switching at 500 kHz offers a wide choice for semiconductors, silicon devices as well as wide band-gap devices are all usable in this frequency range.

C. Pareto Plot

As shown in Fig. 19, tradeoff between high coil link efficiency and power density exists in the IPT coil design. The coil link efficiency is from the primary coil to the secondary coil and exclude the compensation network and converters. The power density is defined as $\frac{2P_{\text{out}}}{(S_p+S_s)d}$, where P_{out} is the output power, S_p and S_s are the surface area of primary and secondary coils, and d is the distance between two coils. The Pareto front for each frequency is clearly visible.

TABLE V
PARAMETERS OF THE PROTOTYPED COILS

Specifications	Characteristics	Prototype I	Prototype II	Prototype III	units
primary coil outer radius	r_{outp}	75	68.5	68.5	mm
primary coil trace width	w_p	10.5	8.6	12.4	mm
primary coil turns gap	s_p	1	2.9	2.9	mm
primary coil turns number	n_p	3	4	3	-
primary coil space-width ratio	$\frac{s_p}{w_p}$	0.1	0.33	0.23	-
primary coil quality factor	Q_p	70.15	61.75	61.75	-
secondary coil outer radius	r_{outs}	75	68.5	55.5	mm
secondary coil trace width	w_s	6.7	4.8	2.9	mm
secondary coil turns gap	s_s	1	1	1	mm
secondary coil turns number	n_s	5	7	6	-
secondary coil space-width ratio	$\frac{s_s}{w_s}$	0.14	0.2	0.34	-
secondary coil quality factor	Q_s	70.7	65.8	56.1	-

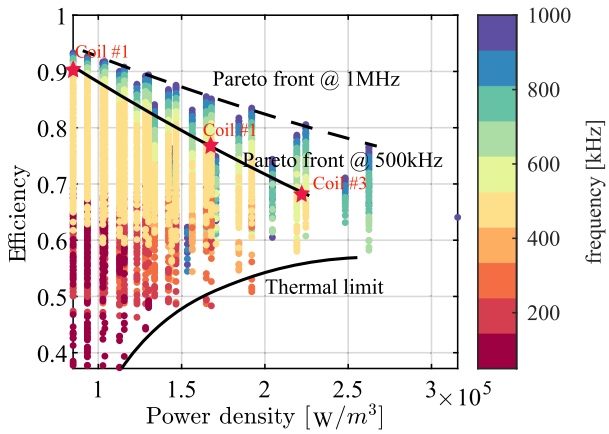

Fig. 19. Pareto plot of the coil link efficiency and power density in the full range of design space. Three designs under a 500-kHz operating frequency are selected for prototyping and marked as star in the figure.

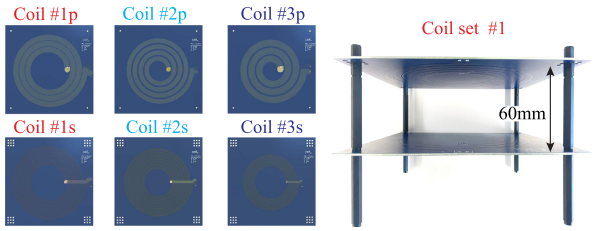

Fig. 20. Top view of six prototype coils and front view of coil set 1 with the primary coil on bottom and the secondary coil on top. Spaces between two coils are controlled by the length of spacers.

VI. EXPERIMENTAL VERIFICATION

In Fig. 19, three designs on the Pareto front of 500 kHz are selected to prototype and the geometries of three coil sets are shown in Table V. Designs are selected to verify different metrics: the coil 1 has the highest efficiency, the coil 3 has the highest power density, and the coil 2 takes the tradeoff between the efficiency and power density into consideration. The prototype of coil pairs is shown in Fig. 20.

TABLE VI
MODELING AND TEST RESULT OF INDUCTANCE AND RESISTANCE OF THREE COIL PAIRS

Coil pair		$L_p[\mu H]$	$L_s[\mu H]$	$R_p[m\Omega]$	$R_s[m\Omega]$	$M[\mu H]$
1	Ana	1.117	3.017	50	134	0.279
	Test	1.12	3.02	48	126	0.274
	Error	$< 1\%$	$< 1\%$	3.6%	6.5%	$< 1\%$
2	Ana	1.18	4.736	60	226	0.302
	Test	1.24	4.74	60	240	0.3
	Error	5.3%	$< 1\%$	$< 1\%$	4.2%	$< 1\%$
3	Ana	0.59	4.129	30	231	0.165
	Test	0.628	4.13	42	195	0.16
	Error	6.5%	$< 1\%$	26%	18%	$< 1\%$

A. Modeling Verification

The inductance and resistance modeling is verified with test using a BK 895 *LCR* meter that has $2\,\%$ accuracy. The test is executed at 500 kHz. The resistance and inductance value obtained from both analytic modeling and test are shown in Table VI. The analytic model of self- and mutual inductance shows a good match with the test results. Large error around 5% appears at large PCB trace width. The largest error of resistance 26% appears at large trace width. This is due to the drop of the resistance model accuracy for large trace width. If looking into the absolute error, 26% of coil resistance corresponds to $12\,\mathrm{m}\Omega$, which is small comparing to parasitic resistance in a peripheral circuit.

The test of mutual inductance under different distances is also performed and results are shown in Fig. 21. The analytic model of mutual inductance shows high accuracy. Moreover, in order to explore the influence of lateral displacement between two coils, which could happen due to wrong installation or vibrations, the test with a lateral displacement of 5 mm in each direction is executed. The misalignment in the direction xy induces the largest discrepancy and its results are shown in Fig. 21. It can be seen that small lateral displacements have a negligible influence on mutual inductance.

B. Power Test

The first coil pair detailed in Table V is tested with a test bench shown in Fig. 22. The coil set is tested with an air gap

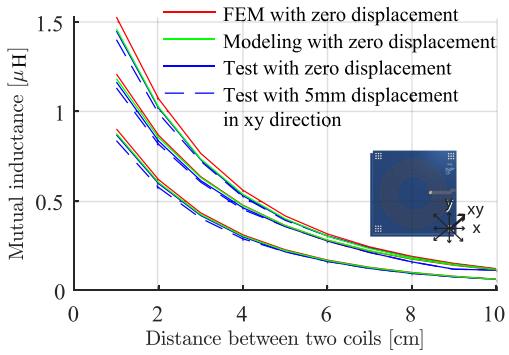

Fig. 21. Mutual inductance for three different coil sets under different transfer air gaps with zero or 5-mm lateral displacement in the xy direction. Along with the increase of the distance between primary and secondary coil, the mutual inductance drops quickly. Test result, FEM result and modeling result correlate well with each other.

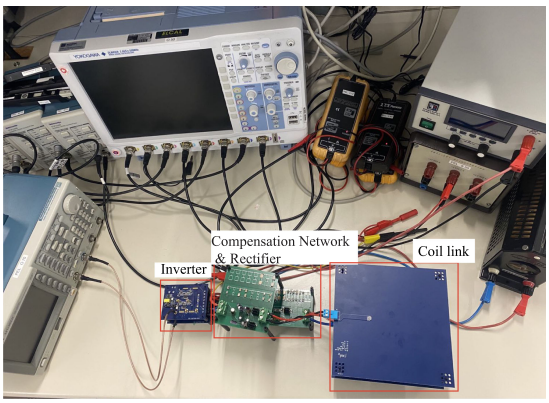

Fig. 22. Test setup of the IPT from 80 V dc input to a resistive load.

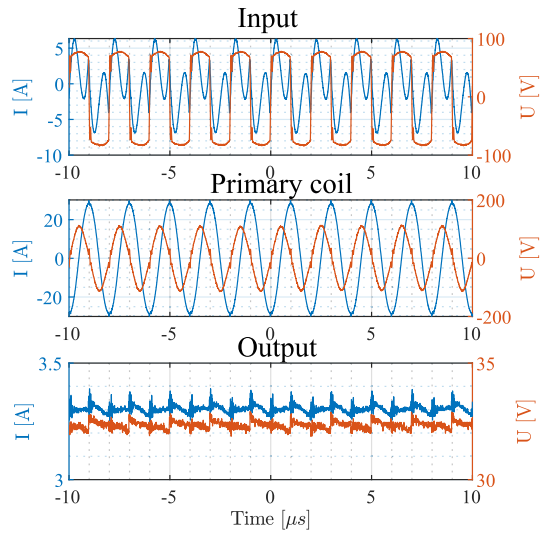

Fig. 23. Power test waveforms for coil pair 1. From top to bottom: 1) voltage and current after a full-bridge inverter; 2) voltage and current across the primary PCB coil; and 3) DC voltage and current after a half-bridge rectifier.

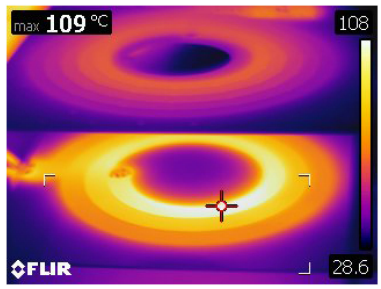

Fig. 24. Thermal image of coils in a steady state.

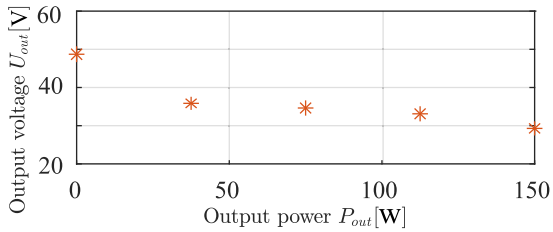

Fig. 25. Output voltage under various load condition for the coil pair 1 with 60-mm air gap between the primary and secondary coils. The load condition changes from the no-load condition to 150 W.

of 60 mm, nominal load of 10 Ω, input voltage of 80 V, and operating frequency of 500 kHz.

Other components in the test bench are as follows. The transmitter coil is connected to a GaN HEMTs-based full-bridge inverter (Infineon, EVAL-1EDF-G1-HB-GAN). The receiver coil is connected to the Schottky-diode-based passive half-bridge rectifier (ST, STPS30M60DJF). Tektronix TCPA300 (dc-100 MHz) current sensors are used to measure the current. Pewatron differential probes are used to measure the voltage. The *LCL* compensation network is used on the primary side and series compensation network is used on the secondary side. TDK MLCC capacitors are used due to their low equivalent series resistance. TDK SPM6550CT type inductors are used for their high power and high-frequency capability.

The current and voltage waveforms for this IPT system are shown in Fig. 23. With an input dc voltage of 80 V, 34 V at output is expected, however, the real output voltage is 33 V. This could be explained by the parasitic resistance in the power loop and error tolerance of compensation components.

The thermal image in the steady state is shown in Fig. 24. It can be seen that the hottest point appears in the innermost turn in the primary coil, which corresponds to the modeling of magnetic field distribution in the coil. According to Fig. 24, the maximum temperature is 109 °C. In our design, the allowed maximum temperature is 125 °C. However, in our thermal model, average temperature is calculated instead of highest temperature and the expected average temperature of the primary coil according to (20) is 99 °C.

Test under different load conditions is executed. As shown in Fig. 25, the output voltage decreases as the output power increases. Load condition influences the output voltage and this is because the nonzero coil resistance would share the secondary induced voltage with load. In the no-load condition, the rectifier on the secondary side is an open circuit. The reflected resistance

of the load to the primary side is now zero, and therefore, the primary current increases. The induced secondary voltage increases accordingly. The current prototype could handle the no-load condition and its minimum load requirement is defined by the insulation voltage on the secondary coil. Above 25% load (37.5 W), the voltage variation is within 6 V, the voltage slope is more or less flat.

In conclusion, a coil prototype considering the application of the auxiliary power supply in MV converters is tested with 80 V dc input, 10 Ω load, 60 mm air gap between primary and secondary coils. 33 V 110 W is obtained at output. The efficiency of the entire IPT system is 67%, including loss on the front and back power electronics converters and on compensation components. Further optimization will be done to improve these numbers.

VII. Conclusion

This article focuses on the PCB coil design in the IPT system for MV applications with a medium power transfer capability and strict insulation requirements. The main contributions of this article are as follows.

First, an improved magnetic field distribution model for coils with rectangular cross sections offers a fast calculation approach. The model is more accurate than the filament method. Second, the proposed model for self- and mutual inductance and resistance can be used to do fast characterization of PCB coils. The accuracy of the model is especially high for trace width below $10\,\mathrm{mm}$. Third, by doing analysis in coil geometries, we found $\frac{s}{w}$ and coil inner radius should not be too large otherwise the coil quality factor would be low. Finally, by simply setting the design specifications and constraints, the proposed design approach could assist users with developed filters, allowing intuitive and easy navigation through a broad design space with high design freedoms. As a demonstration, a coil pair capable of transfering $110\,\mathrm{W}$ via 60 mm air gap is designed and prototyped.

Further ongoing design optimization works are related to the optimization of the IPT coil link as well as the optimization in the power electronics converters and compensation networks for higher efficiency.

References

[1] J. Dai and D. C. Ludois, "A survey of wireless power transfer and a critical comparison of inductive and capacitive coupling for small gap applications," *IEEE Trans. Power Electron.*, vol. 30, no. 11, pp. 6017–6029, Nov. 2015.

[2] M. Schormans, V. Valente, and A. Demosthenous, "Practical inductive link design for Biomedical wireless power transfer: A tutorial," *IEEE Trans. Biomed. Circuits Syst.*, vol. 12, no. 5, pp. 1112–1130, Oct. 2018.

[3] M. Zargham and P. G. Gulak, "Maximum achievable efficiency in near-field coupled power-transfer systems," *IEEE Trans. Biomed. Circuits Syst.*, vol. 6, no. 3, pp. 228–245, Jun. 2020.

[4] P. Si, A. P. Hu, S. Malpas, and D. Budgett, "A frequency control method for regulating wireless power to implantable devices," *IEEE Trans. Biomed. Circuits Syst.*, vol. 2, no. 1, pp. 22–29, Mar. 2008.

[5] S. Y. Choi, B. W. Gu, S. Y. Jeong, and C. T. Rim, "Advances in wireless power transfer systems for roadway-powered electric vehicles," *IEEE J. Emerg. Sel. Topics Power Electron.*, vol. 3, no. 1, pp. 18–36, Mar. 2015.

[6] E. S. Lee, B. G. Choi, M. Y. Kim, and S. H. Han, "Optimal number of turns design of the IPT coils for laptop wireless charging," *IEEE Access*, vol. 9, pp. 19548–19561, Jan. 2021.

[7] K. Kusaka *et al.*, "Galvanic isolation system for multiple gate drivers with inductive power transfer – Drive of three-phase inverter," in *Proc. IEEE Energy Convers. Congr. Expo.*, 2015, pp. 4525–4532.

[8] C. Marxgut, J. Biela, J. W. Kolar, R. Steiner, and P. K. Steimer, "DC-DC converter for gate power supplies with an optimal air transformer," in *Proc. 25th Annu. IEEE Appl. Power Electron. Conf. Expo.*, 2010, pp. 1865–1870.

[9] K. Lee and D. Cho, "Diversity analysis of multiple transmitters in wireless power transfer system," *IEEE Trans. Magn.*, vol. 49, no. 6, pp. 2946–2952, Jun. 2013.

[10] M. J. Chabalko and A. P. Sample, "Three-dimensional charging via multimode resonant cavity enabled wireless power transfer," *IEEE Trans. Power Electron.*, vol. 30, no. 11, pp. 6163–6173, Nov. 2015.

[11] M. A. Houran, X. Yang, and W. Chen, "Magnetically coupled resonance WPT: Review of compensation topologies, resonator structures with misalignment, and EMI diagnostics," *Electronics*, vol. 7, no. 11, pp. 1–45, 2018.

[12] G. R. Nagendra, G. A. Covic, and J. T. Boys, "Determining the physical size of inductive couplers for IPT EV systems," *IEEE J. Emerg. Sel. Topics Power Electron.*, vol. 2, no. 3, pp. 571–583, Sep. 2014.

[13] R. Bosshard, U. Iruretagoyena, and J. W. Kolar, "Comprehensive evaluation of rectangular and double-D coil geometry for 50kW/85kHz IPT system," *IEEE J. Emerg. Sel. Topics Power Electron.*, vol. 4, no. 4, pp. 1406–1415, Dec. 2016.

[14] R. Bosshard, J. Mühlethaler, J. W. Kolar, and I. Stevanović, "Optimized magnetic design for inductive power transfer coils," in *Proc. IEEE 28th Annu. Appl. Power Electron. Conf. Expo.*, 2013, pp. 1812–1819.

[15] S. S. Mohan, "The design, modeling and optimization of on-chip inductor and transformer circuits," Ph.D. dissertation, Dept. Elect. Eng., Stanford Univ., Stanford, CA, USA, pp. 1–215, 1999.

[16] K. Sun, Y. Xu, J. Wang, R. Burgos, and D. Boroyevich, "Insulation design of wireless auxiliary power supply for medium voltage converters," *IEEE J. Emerg. Sel. Topics Power Electron.*, vol. 9, no. 4, pp. 4200–4211, Aug. 2021.

[17] S. Mohan, M. del M. Hershenson, S. Boyd, and T. Lee, "Simple accurate expressions for planar spiral inductances," *IEEE J. Solid-State Circuits*, vol. 34, no. 10, pp. 1419–1424, Oct. 1999.

[18] I. Lope, C. Carretero, J. Acero, R. Alonso, and J. M. Burdío, "AC power losses model for planar windings with rectangular cross-sectional conductors," *IEEE Trans. Power Electron.*, vol. 29, no. 1, pp. 23–28, Jan. 2014.

[19] O. C. Spro *et al.*, "Optimized design of multi-MHz frequency isolated auxiliary power supply for gate drivers in medium-voltage converters," *IEEE Trans. Power Electron.*, vol. 35, no. 9, pp. 9494–9509, Sep. 2020.

[20] K. van Schuylenbergh and R. Puers, *Inductive Powering: Basic Theory and Application to Biomedical Systems(Analog Circuits and Signal Processing)*. Dordrecht, The Netherlands: Springer, 2009.

[21] X. Du and D. Dujić, "Inductive power transfer system with series connected primary and independent secondary coils," in *Proc. 46th Annu. Conf. IEEE Ind. Electron. Soc.*, 2020, pp. 3901–3906.

[22] *IEC 61800-5-1: Adjustable Speed Electrical Power Drive Systems—Part 5-1: Safety Requirements—Electrical, Thermal and Energy*, CENELEC EN 61800-5-1, 2007.

[23] S. Babic and C. Akyel, "New analytic-numerical solutions for the mutual inductance of two coaxial circular coils with rectangular cross section in air," *IEEE Trans. Magn.*, vol. 42, no. 6, pp. 1661–1669, Jun. 2006.

[24] W. Kuhn and N. Ibrahim, "Analysis of current crowding effects in multiturn spiral inductors," *IEEE Trans. Microw. Theory Techn.*, vol. 49, no. 1, pp. 31–38, Jan. 2001.

[25] R. Bosshard, J. W. Kolar, J. Mühlethaler, I. Stevanović, B. Wunsch, and F. Canales, "Modeling and η - α - pareto optimization of inductive power transfer coils for electric vehicles," *IEEE J. Emerg. Sel. Topics Power Electron.*, vol. 3, no. 1, pp. 50–64, Mar. 2015.

[26] M. Q. Nguyen, Z. Hughes, P. Woods, Y. Seo, S. Rao, and J. Chiao, "Field distribution models of spiral coil for misalignment analysis in wireless power transfer systems," *IEEE Trans. Microw. Theory Techn.*, vol. 62, no. 4, pp. 920–930, Apr. 2014.

[27] E. B. Rosa and F. W. Grover, *Formulas and Tables for the Calculation of Mutual and Self-Inductance*, U.S. Government Printing Office, Washington, DC, USA, pp. 1–237, 1912.

[28] M. Mogorovic and D. Dujic, "100kW, 10kHz medium-frequency transformer design optimization and experimental verification," *IEEE Trans. Power Electron.*, vol. 34, no. 2, pp. 1696–1708, Feb. 2019.

[29] C. Zierhofer and E. Hochmair, "Geometric approach for coupling enhancement of magnetically coupled coils," *IEEE Trans. Biomed. Eng.*, vol. 43, no. 7, pp. 708–714, Jul. 1996.

[30] *2221A: Generic Standard on Printed Board Design*, IPC Standard IPC-2221A, 1998

[31] S. Mehri, A. C. Ammari, J. Slama, and M. Sawan, "Minimizing printed spiral coil losses for inductive link wireless power transfer," in *Proc. IEEE Wireless Power Transf. Conf.*, 2016, pp. 1–4.

Xiaotong Du (Student Member, IEEE) received the B.Sc. and M.Sc. degrees from Xi'an Jiaotong University, Xi'an, China, in 2016 and 2019, respectively, and the Dipl.-Ing. degree from École Centrale de Nantes, Nantes, France, in 2019. She is currently working toward the Ph.D. degree with École Polytechnique Fédérale de Lausanne (EPFL), Lausanne, Switzerland.

During the B.Sc. degree, she spent two years with École Centrale de Nantes, as a double degree program student. In 2019, she joined Power Electronics Laboratory, EPFL, as a Doctoral Research Assistant. Her research interests include modeling, design, and optimization of inductive power transfer and resonant converters.

Chengmin Li (Member, IEEE) received the B.S. degree in electrical engineering from the School of Electrical and Electronic Engineering, Huazhong University of Science and Technology, Wuhan, China, in 2013, and the Ph.D. degree from Zhejiang University, Hangzhou, China, in 2019.

From March 2016 to March 2017, he was a Research Intern with GE Global Research Center, Shanghai, China. Since 2020, he has been a Postdoctoral Researcher with Power Electronics Laboratory, École Polytechnique Fédérale de Lausanne, Lausanne, Switzerland. His research interests include medium-voltage high-power converters and applications of SiC power MOSFETs.

Dražen Dujić (Senior Member, IEEE) received the Dipl.-Ing. and M.Sc. degrees from the University of Novi Sad, Novi Sad, Serbia, in 2002 and 2005, respectively, and the Ph.D. degree from Liverpool John Moores University, Liverpool, U.K., in 2008, all in electrical engineering.

From 2002 to 2006, he was with the Department of Electrical Engineering, University of Novi Sad, as a Research Assistant. From 2006 to 2009, he was with Liverpool John Moores University, as a Research Associate. From 2009 to 2013, he was with the ABB Corporate Research Centre, Switzerland, as a Principal Scientist, working on the power electronics projects spanning the range from low-voltage/power switch-mode power supply in below kilowatt range to medium-voltage high-power converters in a megawatt range. From 2010 to 2011, he was a member of a project team responsible for the development of the world's first power electronic traction transformer successfully commissioned on the locomotive. From 2013 to 2014, he was with ABB Medium Voltage Drives, Turgi, Switzerland, as a Research and Development Platform Manager, responsible for ABB's largest IGCT-based medium-voltage drive ACS6000. He is currently with École Polytechnique Fédérale de Lausanne, Lausanne, Switzerland, as an Associate Professor and the Director with Power Electronics Laboratory. He has authored or co-authored more than 200 scientific publications and has led 18 patents. His current research interests include the areas of design and control of advanced high-power electronics systems for medium-voltage applications.

Dr. Dujić was the recipient of the First Prize Paper Award from the Electric Machines Committee of the IEEE Industrial Electronics Society, in 2007; the Isao Takahashi Power Electronics Award for outstanding achievement in power electronics, in 2014; and the EPE Outstanding Service Award from the European Power Electronics and Drives Association in 2018. He is an Associate Editor for the IEEE TRANSACTIONS ON INDUSTRIAL ELECTRONICS, the IEEE TRANSACTIONS ON POWER ELECTRONICS, and the *IET Electric Power Applications*.